Environmental Pollution 390 (2026) 127445

Contents lists available at ScienceDirect

Environmental Pollution

journal homepage: www.elsevier.com/locate/envpol

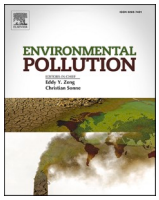

Are all nanoplastics equally neurotoxic? Influence of size and surface functionalization on the toxicity of polystyrene nanoplastics in human neuronal cells☆

Carolina Mota [a], Ana Margarida Araújo [a,*], Maria Enea [b,1], Eulália Pereira [b], Ana Reis-Mendes [a], Rui Fernandes [c], Sofia Pacheco [c], Marlene Lúcio [d], Carla Martins Lopes [e,f,g], Isabel M.P.L.V.O. Ferreira [a], Márcia Carvalho [a,f,g,**]

[a] LAQV/REQUIMTE, Laboratory of Bromatology and Hydrology, Department of Chemical Sciences, Faculty of Pharmacy, University of Porto, 4050-313, Porto, Portugal
[b] LAQV/REQUIMTE, Laboratory for Green Chemistry, Departament of Chemistry and Biochemistry, Faculty of Sciences, University of Porto, 4169-007, Porto, Portugal
[c] HEMS-Histology and Electron Microscopy, Instituto de Investigação e Inovação em Saúde (I3S), University of Porto, Porto, Portugal
[d] CF-UM-UP, Center of Physics of the Universities of Minho and Porto, LaPMET, Laboratory of Physics for Materials and Emergent Technologies and CBMA, Center of Molecular and Environmental Biology, University of Minho, 4710-057, Braga, Portugal
[e] Associate Laboratory i4HB—Institute for Health and Bioeconomy; UCIBIO—Applied Molecular Biosciences Unit, MEDTECH, Laboratory of Pharmaceutical Technology, Department of Drug Sciences, Faculty of Pharmacy, University of Porto, Porto, Portugal
[f] Instituto de Investigação, Inovação e Desenvolvimento Fernando Pessoa (FP-I3ID), Fernando Pessoa University, Fernando Pessoa Teaching and Culture Foundation, 4249-004 Porto, Portugal
[g] RISE-Health, Faculty of Health Sciences, Fernando Pessoa University, Fernando Pessoa Teaching and Culture Foundation, 4200-150, Porto, Portugal

ARTICLE INFO

Keywords:
Polystyrene nanoplastics
SH-SY5Y
Neuronal toxicity
Functional groups
Size

ABSTRACT

Nanoplastics (NPs) are an emerging environmental concern, particularly due to their potential interactions with the nervous system. We evaluated the neurotoxic effects of four types of polystyrene nanoplastics (PS-NPs): unmodified (plain) 50 nm and 100 nm particles, and 100 nm particles functionalized with carboxyl (C-NPs) or amine (A-NPs) groups. Human SH-SY5Y neuroblastoma cells were exposed to 1–500 μg/mL for 24 or 48 h. Dynamic light scattering revealed aggregation of plain 50 nm NPs in water, while presence of ≥1 % fetal bovine serum improved colloidal stability across all particle types. Zeta potentials in water were approximately −45 mV for plain and C-NPs and −30 mV for A-NPs. In complete medium, all values shifted toward −20 to −13 mV, consistent with protein corona formation. Integrating colloidal stability, surface chemistry, and organelle-level analyses, we established a unified mechanistic framework for PS-NP neurotoxicity. Toxicity endpoints included cell viability, ROS/RNS generation, particle internalization, and morphological and ultrastructural analysis. Plain PS-NPs showed negligible cytotoxicity, whereas C-NPs and especially A-NPs significantly reduced cell viability. A-NPs caused a 21–41 % reduction at 100–500 μg/mL after 24 h, and 29–66 % at 200–500 μg/mL after 48 h ($p = 0.0007$ vs. C-NPs). ROS/RNS levels were highest with plain 100 nm and A-NPs at ≥200 μg/mL, increasing over time. Transmission electron microscopy revealed size- and surface chemistry-dependent damage, including endoplasmic reticulum dilation, Golgi fragmentation, and mitochondrial abnormalities. Internalization followed the trend A-NPs > C-NPs ≫ plain PS-NPs, mirroring organelle damage, apoptosis, autophagy, and lysosomal disruption. These findings identify surface chemistry, more than particle size, as the primary driver of PS-NP neurotoxicity, highlighting its importance for risk prioritization and regulatory frameworks addressing NP hazards.

☆ This paper has been recommended for acceptance by Dr Mingliang Fang.

* Corresponding author.
** Corresponding author. LAQV/REQUIMTE, Laboratory of Bromatology and Hydrology, Department of Chemical Sciences, Faculty of Pharmacy, University of Porto, 4050-313, Porto, Portugal
E-mail addresses: amaraujo@ff.up.pt (A.M. Araújo), mcarv@ufp.edu.pt (M. Carvalho).
[1] Present address: NanoSafety Group, International Iberian Nanotechnology Laboratory, 4715-330 Braga, Portugal.

https://doi.org/10.1016/j.envpol.2025.127445
Received 26 August 2025; Received in revised form 18 October 2025; Accepted 25 November 2025
Available online 26 November 2025

1. Introduction

Plastics have revolutionized modern life, becoming indispensable in agriculture, healthcare, packaging, construction, and technology (Patil et al., 2022; Pironti et al., 2021). However, they persist for centuries, fragmenting into microplastics (MPs, <5 mm) and nanoplastics (NPs, <1 μm) (Shi et al., 2022). These particles arise from primary sources (e.g., microbeads in personal care products) or secondary degradation, exhibiting variability in size, shape, and polymer composition (Guo et al., 2022; Kadac-Czapska et al., 2024). The polymeric composition of NPs dictates their environmental behavior and health effects. Polystyrene (PS), widely used in single-use products, food containers, insulation, and packaging, is of concern due to its tendency to fragment into nanoscale particles (Hu et al., 2022; Hwang et al., 2020).

The toxicological impact of MPs/NPs is aggravated by chemical additives (plasticizers, stabilizers) and their capacity to adsorb pollutants such as PAHs, pesticides, and pharmaceuticals (He et al., 2022; Verla et al., 2019). Adsorption depends on particle size, surface area, polarity, and aging (Fu et al., 2021). Larger or high–surface area particles retain more contaminants (Enders et al., 2015; Zhang et al., 2019), whereas aging may reduce capacity (Fu et al., 2021). Non-polar polymers (PE, PP, PS) show higher affinity for pollutants than polar polymers (PVC, PC), enhancing their role as vectors of toxic compounds (Liu et al., 2019).

Human exposure to NPs occurs mainly via ingestion, with inhalation and dermal routes as additional pathways (Jin et al., 2021; Kadac-Czapska et al., 2024; Liu et al., 2021). NPs have been detected in seafood, fruits, vegetables, and beverages (Jin et al., 2021; Liu et al., 2021; Vitali et al., 2023; Ziani et al., 2023; Zolotova et al., 2022), contributing to estimated intakes of 0.1–5 g weekly (Kadac-Czapska et al., 2024). Once absorbed, NPs translocate via the bloodstream and accumulate in organs including liver, kidneys, spleen, lungs, placenta, and brain (Feng et al., 2023). Neurotoxicity is particularly concerning, as NPs cross the blood–brain barrier (BBB) and accumulate in brain tissues (Bai et al., 2024; Y. Ma et al., 2024; Prüst et al., 2020; Shan et al., 2022). A recent study confirmed their presence in the human brain (Nihart et al., 2025). NP neurotoxicity depends on particle size, surface properties, and functionalization, which influence uptake and biomolecular interactions (Abbasi et al., 2023; Conesa & Iñiguez, 2020). Smaller PS-NPs (e.g., 50 nm) can be internalized by endothelial cells, inducing oxidative stress, inflammation, and BBB disruption (Shan et al., 2022). Functionalized NPs (e.g., –COOH, $–NH_2$) interact distinctly with biological systems, potentially exacerbating neurotoxic effects via altered signaling and membrane disruption (Y. Ma et al., 2024; Shi et al., 2022). Yet, the neurotoxicity of functionalized NPs remains underexplored.

Another key factor is the protein corona, formed when biomolecules adsorb to NP surfaces in biological fluids (Kopac, 2021). Its composition depends on NP size, shape, charge, and functionalization, altering uptake, distribution, and toxicity (Akhter et al., 2021). In vitro, fetal bovine serum (FBS) is widely used to mimic physiological conditions, but concentrations markedly affect NP stability and aggregation (Anders et al., 2015). Thus, understanding serum effects is essential for accurate neurotoxicity assessment.

This study addresses these gaps by: (1) assessing PS-NP stability in media with varying FBS concentrations; (2) investigating uptake and morphological alterations in SH-SY5Y neuronal cells; and (3) evaluating the role of surface functionalization in PS-NP-induced neurotoxicity. Collectively, these investigations advance understanding of PS-NP neurotoxicity and its potential health impacts.

2. Material and methods

2.1. Nanoplastics and reagents

PS-NPs were purchased from Polysciences Europe GmbH (Hirschberg, Germany). Plain PS-NPs were supplied in two sizes: 50 nm (P-NPs 50) and 100 nm (P-NPs 100). Functionalized PS-NPs—carboxylate-modified (C-NPs 100) and amino-modified (A-NPs 100)—were 100 nm in diameter. All were provided as 2.5 % (w/v) aqueous suspensions, with particle concentrations of 3.64×10^{14}/mL (50 nm) and 4.55×10^{13}/mL (100 nm). The coefficient of variation (CV) was 15 % for all NP types, except A-NPs 100 (25 %).

Dimethyl sulfoxide (DMSO, >99.9 %) and MTT (>98 %) were obtained from Duchefa Biochemie B.V. (Haarlem, Netherlands). DCFDA, Triton X-100, Hoechst 33342, and propidium iodide (PI) were from Sigma Aldrich (St. Louis, MO, USA). Paraformaldehyde 4 % was purchased from Alfa Aesar (Kandel, Germany). Dulbecco's Modified Eagle Medium (DMEM), fetal bovine serum (FBS), penicillin/streptomycin (Pen/Strep), Trypsin-EDTA (0.25 %/0.02 %), and Hanks' Balanced Salt Solution (HBSS) were from BIOWEST (Nuaillé, France).

For TEM, glutaraldehyde (#16316), formaldehyde (#15713), osmium tetroxide (#19190), Embed-812 resin (#14120), uranyl acetate substitute (#22409), lead citrate (#22410), and copper grids were obtained from Electron Microscopy Sciences (Hatfield, England). The RMC Ultramicrotome was from PowerTome (USA), and the JEOL JEM 1400 TEM from JEOL (Tokyo, Japan).

2.2. Polystyrene nanoplastics' characterization

Dynamic Light Scattering (DLS) was used to characterize PS-NPs size and evaluate the influence of FBS content on stability over time. Commercial NPs suspensions were sonicated for 10 min, and 1 mg/mL solutions prepared in culture medium with varying FBS concentrations (0 %, 1 %, 5 % or 10 %, v/v). Samples in ultrapure water and culture medium without FBS were immediately analyzed to assess the initial particle size distribution. Stability was evaluated by incubating samples at 37 °C with 5 % CO_2, and 100 % relative humidity, with measurements at 24 and 48 h. Key parameters measured included the size (diameter obtained from an intensity distribution or number distribution), polydispersity index (PDI, indicating size variability), and zeta potential (correlated with surface charge). A PDI below 0.3 suggests uniform size distribution, while higher values indicate greater variability or aggregation. Increases in PDI and size (intensity distribution) were interpreted as aggregation (Tallec et al., 2019). Measurements were conducted in triplicate using a Malvern Instruments device, each replicate comprising 13 runs of 10 s each. The Anton Paar Litesizer® 500 (Anton Paar GmbH, Graz, Austria) was used to evaluate zeta potential. To avoid multiple scattering from high particle concentration, NP suspensions were sonicated for 1 min and diluted (1:400) with purified water (v:v) or DMEM (0 %, 1 %, 5 %, or 10 % of FBS), achieving the desired scattering intensity (i.e. count rate of 250–500, minimal attenuation and transmittance >80 %). Experiments were conducted at 25 ± 1 °C in disposable polystyrene cuvettes (KartellLabware, Noviglio, Italy for size) or Univette (Anton Paar GmbH, Graz, Austria used for zeta potential). The zeta potential was determined from electrophoretic mobility using the Helmholtz-von Smoluchowski approximation.

2.3. Cell culture

The human neuroblastoma SH-SY5Y cell line was obtained from the Deutsche Sammlung von Mikroorganismn und Zellkulturen (DSMZ, ACC 209, LOT 17) and maintained at passage numbers below 15 to preserve their neuronal profile. SH-SY5Y cells were cultured in high-glucose DMEM, supplemented with 10 % FBS and 100 U/ml Pen/Strep, and maintained at 37 °C in a 5 % CO_2 incubator. For maintenance, cells were split once a week at ~80 % confluence.

2.4. Cell viability assay

The impact of PS-NPs on SH-SY5Y cell viability was assessed using the MTT assay. Cells were seeded in 48-well plates at a density of 3×10^5 cells/mL and allowed to adhere for 24 h. Cells were then exposed to

plain or functionalized PS-NPs at concentrations ranging from 1 to 500 μg/mL, selected based on commonly tested levels in *in vitro* cytotoxicity studies (Huang et al., 2023; Tang et al., 2022; Lin et al., 2022; Xu et al., 2019; Liu et al., 2022; Ma et al., 2024). Exposure periods of 24 and 48 h were chosen to capture both acute and time-dependent cellular responses, consistent with prior NP neurotoxicity studies (Ban et al., 2021; Huang et al., 2023; Lin et al., 2022; Domenech et al., 2021; Yang et al., 2023), allowing sufficient NP–cell interaction while avoiding nutrient depletion or stress from prolonged culture. Following exposure, the medium was removed and replaced with 250 μL of MTT solution (0.5 mg/mL). Plates were incubated at 37 °C with 5 % CO_2 in the dark for 2 h. The supernatant was then discarded, and the resulting purple formazan crystals were dissolved in 200 μL of DMSO. Absorbance was measured at 545 and 630 nm using a microplate reader (Stat Fax 3200, Awareness Technology, USA). All measurements were performed in duplicate in at least three independent experiments. Cell viability data were normalized to the untreated control (0 % effect) and to 1 % Triton X-100–treated cells (100 % effect), which served as the maximum cytotoxicity reference for normalization. The Triton-treated condition was used as a fixed benchmark and is not represented in the plotted concentration-response curves.

2.5. Hoechst/propidium iodide fluorescent staining

To gain deeper insight into the mechanisms of NP-induced cell death, dual fluorescent staining with Hoechst/PI was performed. Apoptotic cells were identified based on chromatin morphology, as described previously (Valente et al., 2012). Hoechst 33342, a cell-permeable nuclear dye, emits blue fluorescence upon binding to DNA, whereas PI, a membrane-impermeable dye, emits red fluorescence in cells with compromised membrane integrity.

SH-SY5Y cells were seeded in 24-well plates at a density of 65×10^4 cells/mL. After 24 h of adhesion, cells were exposed to plain or surface-functionalized PS-NPs (50 or 200 μg/mL) in medium with 1 % FBS for 24 or 48 h. Following exposure, cells were washed with 1 mL HBSS (+/+) containing calcium and magnesium, then incubated with 300 μL PI (10 μM) for 10 min at 37 °C, protected from light. After aspiration and washing, cells were fixed with 300 μL 4 % paraformaldehyde for 15 min, washed again, and incubated with 300 μL Hoechst 33342 (5 μg/mL) for 5 min. After a final wash, 300 μL HBSS were added per well for imaging.

Cells were examined with a Nikon Eclipse TS100 inverted fluorescence microscope using UV-2A (Hoechst; excitation ~350 nm, emission ~460 nm) and G-2A (PI; excitation ~535–590 nm, emission ~615 nm) filter sets. Images were acquired with NIS-Elements software (v5.41.00). Quantitative image analysis was performed using CellProfiler software (version 4.2.8), with at least 2500 cells analyzed per condition to determine the proportion of apoptotic cells.

2.6. Measurement of intracellular reactive oxygen and nitrogen species

Intracellular ROS/RNS generation was evaluated using the DCFH-DA fluorescence assay. SH-SY5Y cells were seeded in 48-well plates and, after overnight adhesion, pre-incubated with 200 μL 0.1 mM DCFDA at 37 °C, protected from light, for 30 min. The probe was then removed, and cells were exposed to plain or functionalized PS-NPs (1–500 μg/mL). Fluorescence was measured at 485 nm excitation/530 nm emission on a Synergy LX Multi-Mode Reader (Bio-Tek, Winooski, VT, USA) after 0.5, 1, 2, 3, 24, and 48 h exposure. Results were normalized to negative controls (cells in culture medium) and expressed as fold increase. All experiments were performed in duplicate in at least three independent replicates.

2.7. Transmission electron microscopy analysis

For ultrastructural analysis, SH-SY5Y cells were seeded in 6-well plates at 30×10^4 cells/mL and allowed to adhere for 24 h before exposure to 50 or 200 μg/mL of each NP type for 24 h. Cells were fixed in 2.5 % glutaraldehyde and 2 % formaldehyde in 0.1 M sodium cacodylate buffer (pH 7.4) for 1 h at room temperature, then post-fixed in 1 % osmium tetroxide. Samples were centrifuged (2000 rpm, 5 min), pellets embedded in Histogel™, washed, stained with 1 % uranyl acetate (30 min), dehydrated through graded ethanol (50–100 %) and propylene oxide, and infiltrated with Embed-812 epoxy resin before polymerization for 48 h at 60 °C. Ultra-thin sections (50 nm) were cut using an RMC Ultramicrotome with Diatome diamond knives, mounted on copper grids, and stained with uranyl acetate substitute and lead citrate (5 min each). Sections were examined with a JEOL JEM 1400 TEM operating at 80 kV, and images captured using a PHURONA camera. TEM analysis was performed at the Histology and Electron Microscopy Service (HEMS), i3S, University of Porto, Portugal.

2.8. Statistical analysis

Results are presented as mean ± standard error of the mean (SEM). Data normality was tested with Shapiro–Wilk. Analyses were conducted separately for each assay. For viability and ROS assays, two-way ANOVA assessed NP type and concentration, followed by Tukey's (pairwise) or Dunnett's (vs. control) post-hoc tests. Nonlinear regression and all calculations were performed with GraphPad Prism 8 (v8.4.3, Mac). Statistical significance was set at $p < 0.05$. Although n-values varied slightly among treatments, independent replicates yielded consistent outcomes, confirming the reliability and reproducibility of the data.

3. Results and discussion

3.1. Physicochemical properties of tested PS-NPs

All four PS-NPs—P-NPs 50, P-NPs 100, C-NPs 100, and A-NPs 100—were characterized to validate and expand manufacturer specifications. Complementary TEM imaging (see Fig. S1) was performed to confirm nanoparticle morphology under dry-state conditions, which, together with DLS data, provides a comprehensive view of both the structural and colloidal behavior of the PS-NPs. DLS was performed in ultrapure water and culture medium without FBS (0 %) at time zero (t = 0 h), with results shown in Fig. S2 and statistical analysis in Table S1 (Supplementary Data).

Hydrodynamic sizes by intensity distribution were generally consistent with manufacturer specifications, with one exception. P-NPs 50 exhibited larger sizes (93 ± 2.0 nm in water; 80 ± 1.1 nm in 0 % FBS) than their nominal 50 nm, suggesting aggregation. This was confirmed by comparing intensity with number distribution measurements (54 ± 2.3 nm in water; 58 ± 1.6 nm in 0 % FBS). In DLS, scattered light intensity scales with particle diameter to the sixth power, so larger particles or aggregates disproportionately influence signals (Bhattacharjee, 2016). In contrast, number distribution gives equal weight to each particle (Souza et al., 2016). Although number distributions for 100 nm PS-NPs (plain and functionalized) yielded mean diameters slightly below 100 nm, this reflects the intrinsic weighting differences in DLS calculations. Number distributions minimize the influence of rare larger particles that dominate intensity-based measurements, often resulting in apparent smaller mean sizes despite actual diameters consistent with manufacturer specifications (Brar & Verma, 2011; Bhattacharjee, 2016; Souza et al., 2016). A substantial discrepancy between intensity and number distributions for P-NPs 50 indicates aggregation, as aggregated systems show larger differences than monodisperse ones (Brar & Verma, 2011). For 100 nm NPs, hydrodynamic sizes matched expected values. A-NPs 100 exhibited slightly larger diameters (120 ± 2.4 nm) than P-NPs 100 (111 ± 1.4 nm) and C-NPs 100 (107 ± 3.6 nm) in 0 % FBS, attributed to hydration shells around amine groups forming hydrogen bonds with water, increasing hydrodynamic size.

All suspensions presented PDI values below 0.2, indicating relatively monodisperse populations (Danaei et al., 2018). However, P-NPs 50

showed the highest PDIs in both media, supporting aggregation.

Fig. S3 shows zeta potential values for the four NP types dispersed in water and in DMEM with varying FBS (0 %, 1 %, 5 %, 10 %); statistics are in Table S2.

Consistent with Y. Ma et al. (2024), plain and functionalized PS-NPs exhibited negative zeta potentials explained by oxidation introducing negatively charged groups (Xu et al., 2024), hydroxyl ion adsorption on polystyrene (Peula-García et al., 2010), and residual sulfate/sulfonate groups from polymerization initiators (Mortensen et al., 2025). The unexpected negative potential of amine-functionalized NPs may reflect incomplete surface coverage, leaving exposed negatively charged regions.

P-NPs and C-NPs showed similar values (ca. −45 mV) in water, while A-NPs showed less negative values (ca. −30 mV). This reflects carboxyl groups being fully deprotonated to COO^- at neutral pH, reinforcing negative charge, while amine groups are partially protonated to NH_3^+, counteracting polystyrene's charge. The pKa and protonation states of surface groups strongly influence zeta potential (Zhang et al., 2022).

In DMEM, PS-NPs showed less divergent zeta potentials (−20 to −13 mV). This narrowing reflects protein corona formation: serum proteins adsorb onto NP surfaces, masking native chemistry and creating a new interface. Albumin and other abundant proteins, negatively charged at physiological pH, dominate surface charge (Monopoli et al., 2012).

Additionally, DMEM salts compress the electrical double layer, reducing potential magnitude regardless of surface functionality (Jiang et al., 2009). High ionic strength screens charges, reducing repulsion and yielding more similar values across NP types (Bhattacharjee, 2016). Medium components (amino acids, vitamins, etc.) further compete for surface sites, altering charge distribution (Allouni et al., 2009).

3.2. *Serum-dependent colloidal behavior of PS-NPs*

The dispersion and stability of PS-NPs *in vitro* are critical determinants of toxicity (Fleischer & Payne, 2014). We assessed their 48 h stability in media containing FBS (0 %, 1 %, 5 %, 10 %), reflecting conditions commonly used in cell studies (Ban et al., 2021; Domenech et al., 2021; Lin et al., 2022; Wang et al., 2022; Xu et al., 2019). Since NPs form protein coronas that alter physicochemical and biological properties (Fleischer & Payne, 2014), understanding this process is essential for interpreting aggregation, uptake, and toxicity (Rahman et al., 2013; Sun et al., 2019).

Hydrodynamic sizes (by intensity) were measured for each condition and time point (Fig. 1), with size and PDI values in Tables S3 and S4 (Supplementary Data).

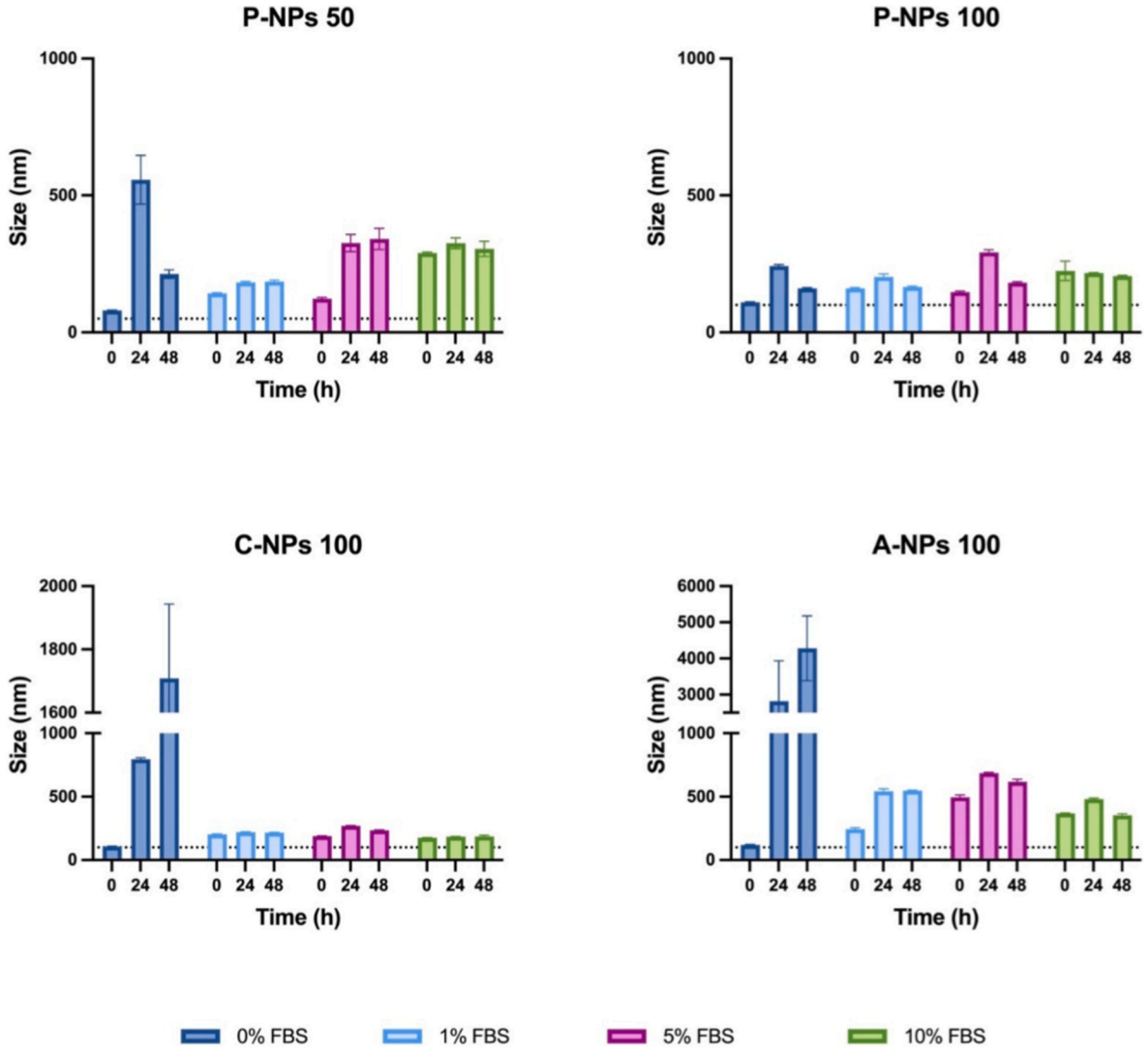

Fig. 1. Effect of FBS concentration and incubation time on PS-NPs stability. Size and dispersity metrics (size distribution by intensity, and PDI) were measured for P-NPs 50, P-NPs 100, C-NPs 100, and A-NPs 100 dispersed in DMEM with varying FBS concentrations (0 %, 1 %, 5 %, 10 %) over 48h. Data are presented as mean ± standard error of the mean (SEM) (n = 3).

PS-NPs were unstable in serum-free medium, showing progressive aggregation due to electrolytes compressing the electrical double layer, reducing repulsion, and allowing van der Waals forces to dominate (Monopoli et al., 2012). Without proteins, particles lacked corona-derived stabilization: (i) steric hindrance, (ii) charge modification by negatively charged albumin, and (iii) increased hydrophilicity (Monopoli et al., 2012).

Addition of 1 % FBS markedly improved stability by forming sufficient corona, providing optimal steric and electrostatic stabilization (Yeo et al., 2015). At higher FBS (5 %, 10 %), multilayer adsorption and protein–protein interactions likely reduced stability compared to 1 %. Thus, 1 % FBS was selected for subsequent assays, balancing stability with minimal interference. Cells were maintained under 10 % FBS during growth and pre-exposure conditions to ensure optimal viability, and the reduction to 1 % FBS was applied only during the exposure period to maintain physiological relevance while preserving assay sensitivity.

3.3. Cytotoxic hierarchy reflects size and, above all, surface functionality

Although the NP concentrations used in this study exceed current environmental estimates (Maity et al., 2022; Materić et al., 2022; Okoffo and Thomas, 2024; Süssmann et al., 2026; Yang et al., 2021) and recently reported human exposure levels (Brits et al., 2024; Ji et al., 2025; Leslie et al., 2022), these ranges are widely applied *in vitro* to elucidate concentration-dependent mechanisms and to support hazard characterization under controlled conditions (Huang et al., 2023; Tang et al., 2022; Lin et al., 2022; Xu et al., 2019; Liu et al., 2022; L. Ma et al., 2024). Figs. 2 and 3 present the cytotoxic effects of the four PS-NP types on SH-SY5Y cells after 24 and 48 h exposures.

Plain NPs (P-NPs 50, 100) exhibited minimal cytotoxicity. P-NPs 50 at 10 μg/mL modestly but significantly increased viability at 24 h (Fig. 2A and B), suggesting a hormetic response, which disappeared by 48 h (Fig. 3A and B). Higher P-NPs 50 concentrations and all P-NPs 100 concentrations had no effect. A significant difference between P-NPs 50 and 100 was observed at 24 h ($p < 0.0001$; Fig. 2C) but not at 48 h ($p > 0.05$; Fig. 3C).

In contrast, functionalized NPs induced marked, concentration- and time-dependent cytotoxicity ($p < 0.0001$; Fig. 2A–B, 3A-B). C-NPs 100 reduced viability by up to 40 % (24 h) and 58 % (48 h). A-NPs 100 were more toxic, reducing viability by 41 % and 66 % at the same time points. At 48 h, A-NPs were significantly more toxic than C-NPs ($p = 0.0007$; Fig. 3C), though no difference was observed at 24 h. Both functionalized NPs were consistently more cytotoxic than plain NPs at all times ($p < 0.0001$; Figs. 2C and 3C).

These results highlight surface functionalization as a key modulator of cytotoxicity. The hormetic-like increase at low P-NPs 50 concentrations aligns with prior neuronal (Huang et al., 2023; Tang et al., 2022) and non-neuronal reports (Lin et al., 2022; Xu et al., 2019), suggesting protective responses under mild stress, though not sustained. Our findings agree with Y. Ma et al. (2024) for P-NPs 100 in SH-SY5Y cells but contrast with studies reporting higher toxicity of plain PS-NPs (Huang et al., 2023; Shi et al., 2022), likely due to formulation differences such as surfactants (Petersen et al., 2022).

The pronounced toxicity of A-NPs 100 matches findings in mouse C17.2 cells (Shi et al., 2022; Yang et al., 2023) and correlates with efficient internalization, driven by their positive charge promoting electrostatic interactions with negatively charged membrane phosphates (Banerjee et al., 2021; Li & Malmstadt, 2013). C-NPs 100 also showed notable uptake but less than A-NPs. P-NPs 50 unexpectedly showed lower uptake, despite smaller size usually favoring entry (Huang et al., 2023; Tang et al., 2022). Our stability data revealed their

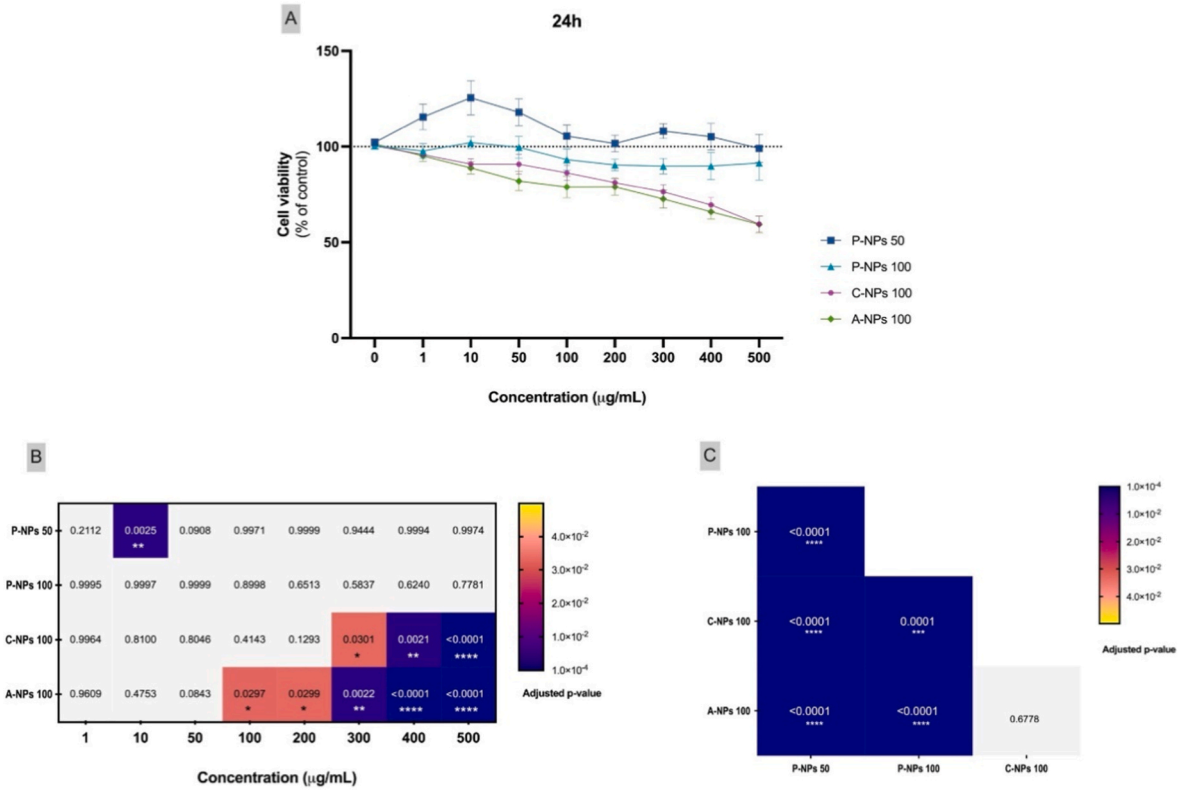

Fig. 2. Cytotoxic effects of plain and functionalized PS-NPs in SH-SY5Y cells after 24-h exposure. **(A)** Cell viability assessed by MTT assay after exposure to 1–500 μg/mL of plain PS-NPs (P-NPs 50 and P-NPs 100) and functionalized PS-NPs (C-NPs 100 and A-NPs 100). Data are presented as mean ± standard error of the mean (SEM) ($n = 4$, except $n = 6$ for P-NPs 50). **(B)** Heatmap depicting statistical significance of differences between treated and control (medium 1 % FBS, no NPs) groups. **(C)** Heatmap comparing viability across PS-NP types. *$p < 0.05$ (yellow), **$p < 0.01$, ***$p < 0.001$ and ****$p < 0.0001$ (dark blue); grey represents non-significance ($p > 0.05$). (For interpretation of the references to color in this figure legend, the reader is referred to the Web version of this article.)

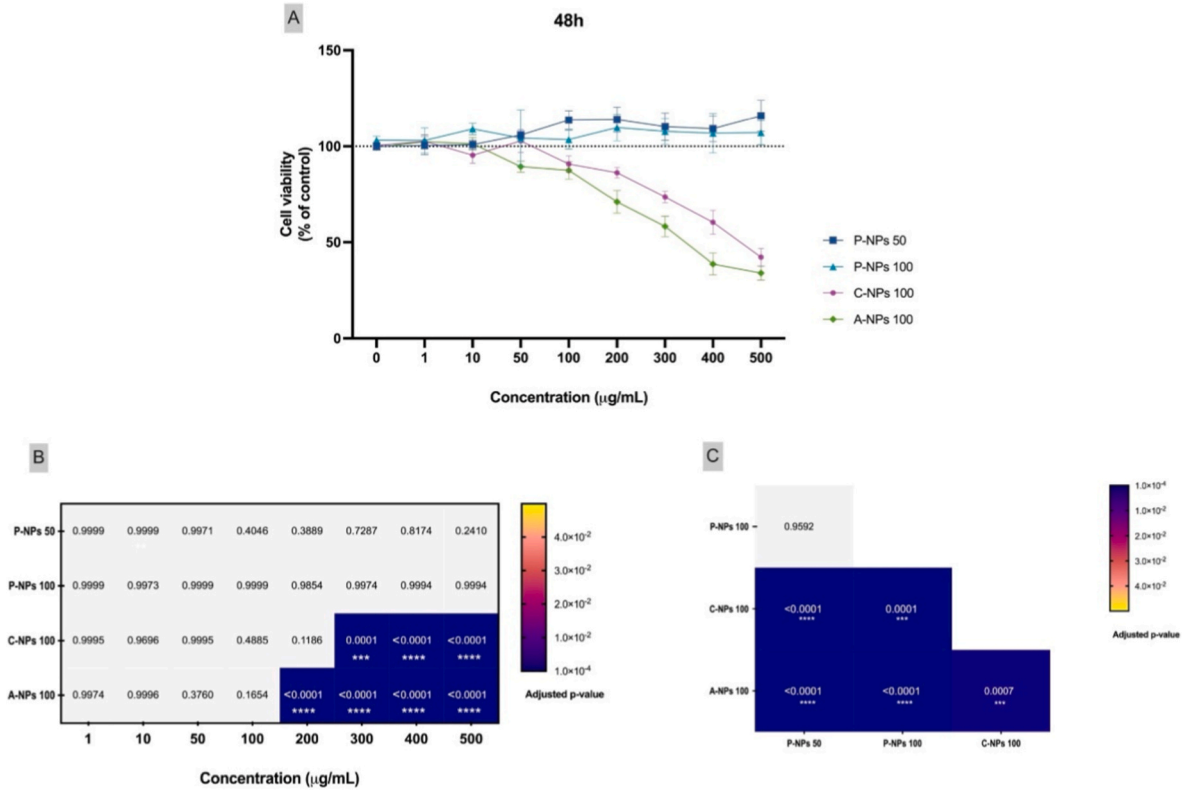

Fig. 3. Cytotoxic effects of plain and functionalized PS-NPs in SH-SY5Y cells after 48-h exposure. **(A)** Cell viability assessed by MTT assay following exposure to 1–500 μg/mL of plain PS-NPs (P-NPs 50 and P-NPs 100) and functionalized PS-NPs (C-NPs 100 and A-NPs 100). Data are presented as mean ± standard error of the mean (SEM) (n = 3 for plain NPs; n = 5 for C-NPs 100 and n = 6 for A-NPs 100). **(B)** Heatmap depicting statistical significance of differences between NP-treated groups and control (medium 1 % FBS, no NPs). **(C)** Heatmap comparing viability across PS-NP types. *p < 0.05 (yellow), **p < 0.01, ***p < 0.001 and ****p < 0.0001 (dark blue); grey represents non-significance (p > 0.05). (For interpretation of the references to color in this figure legend, the reader is referred to the Web version of this article.)

aggregation into larger clusters, likely limiting entry.

Fluorescence microscopy confirmed apoptosis as the predominant cell death pathway. SH-SY5Y cells, either untreated or exposed to NPs, were stained with Hoechst 33342 and PI. Representative images after 48 h and the corresponding quantification of apoptotic cells are presented in Fig. S4 (Supplementary Data). Apoptotic nuclei were identified by bright Hoechst fluorescence, indicative of chromatin condensation and nuclear fragmentation, whereas PI stained necrotic or late-apoptotic cells with compromised membrane integrity (Kari et al., 2022). Control cells exhibited intact, uniformly stained nuclei, while NP-treated cells showed increased numbers of PI-positive nuclei and apoptotic condensation, most pronounced for amine- and carboxyl-modified NPs (Fig. S4). These observations are consistent with MTT assay results, supporting the higher cytotoxicity of functionalized PS-NPs.

3.4. Differential redox responses to distinct PS-NP types

To evaluate oxidative stress, intracellular ROS and RNS were measured at multiple time points (0.5–48 h); only 24- and 48-h results with significant effects are shown in Fig. 4. ROS/RNS patterns varied by NP type and concentration, with broadly similar trends across time points but clearer differences after longer exposure, particularly for amine-functionalized NPs.

At 24 h, P-NPs 50 and C-NPs 100 showed no significant ROS/RNS changes, indicating no redox disruption. P-NPs 100 displayed a biphasic response: a slight decrease at 1–100 μg/mL, followed by concentration-dependent increases at 300–500 μg/mL, significant at 500 μg/mL. A-NPs 100 also increased ROS/RNS, but only at 500 μg/mL.

By 48 h, these trends persisted: P-NPs 50 and C-NPs 100 remained inactive, P-NPs 100 maintained the biphasic pattern, and A-NPs 100 triggered stronger increases at 400–500 μg/mL.

Oxidative stress is often implicated in NP-induced neuronal toxicity (Liu et al., 2022; Tang et al., 2022). Our findings partly support this, as P-NPs 100 significantly increased ROS/RNS at high concentrations, consistent with Liu et al. (2022) in mouse hippocampal HT22 cells. In contrast, P-NPs 50 had negligible effects, likely due to low uptake and reduced interaction with ROS/RNS-producing pathways. A slight non-significant decrease at low concentrations also mirrored the hormesis effect seen in viability assays.

Oxidative stress induction was further modulated by surface functionalization. A-NPs, but not C-NPs, significantly elevated ROS/RNS at high concentrations. Notably, both C-NPs 100 and A-NPs 100 caused cytotoxicity without ROS/RNS increases at 100–200 μg/mL, suggesting oxidative stress is not the sole toxicity mechanism. This contrasts with Yang et al. (2023), who found only A-NPs induced both cytotoxicity and ROS in mouse C17.2 neuronal progenitors. In our study, both functionalized NPs induced cytotoxicity, indicating toxicity may strongly depend on cell type.

3.5. Cellular uptake and organelle-level toxicity

TEM was used to assess PS-NP internalization and ultrastructural alterations in SH-SY5Y cells following 24 h exposure to P-NPs (50, 100 nm), A-NPs 100, and C-NPs 100 (50 and 200 μg/mL). Representative images are shown in Fig. 5, and a semi-quantitative summary of the observed morphological changes is presented in Table 1. All PS-NPs were internalized via endocytosis, localizing mainly within endosome-like vesicular structures. Uptake was strongly influenced by surface functionalization: A-NPs 100 showed the highest intracellular counts, followed by C-NPs 100, while plain NPs showed the lowest uptake.

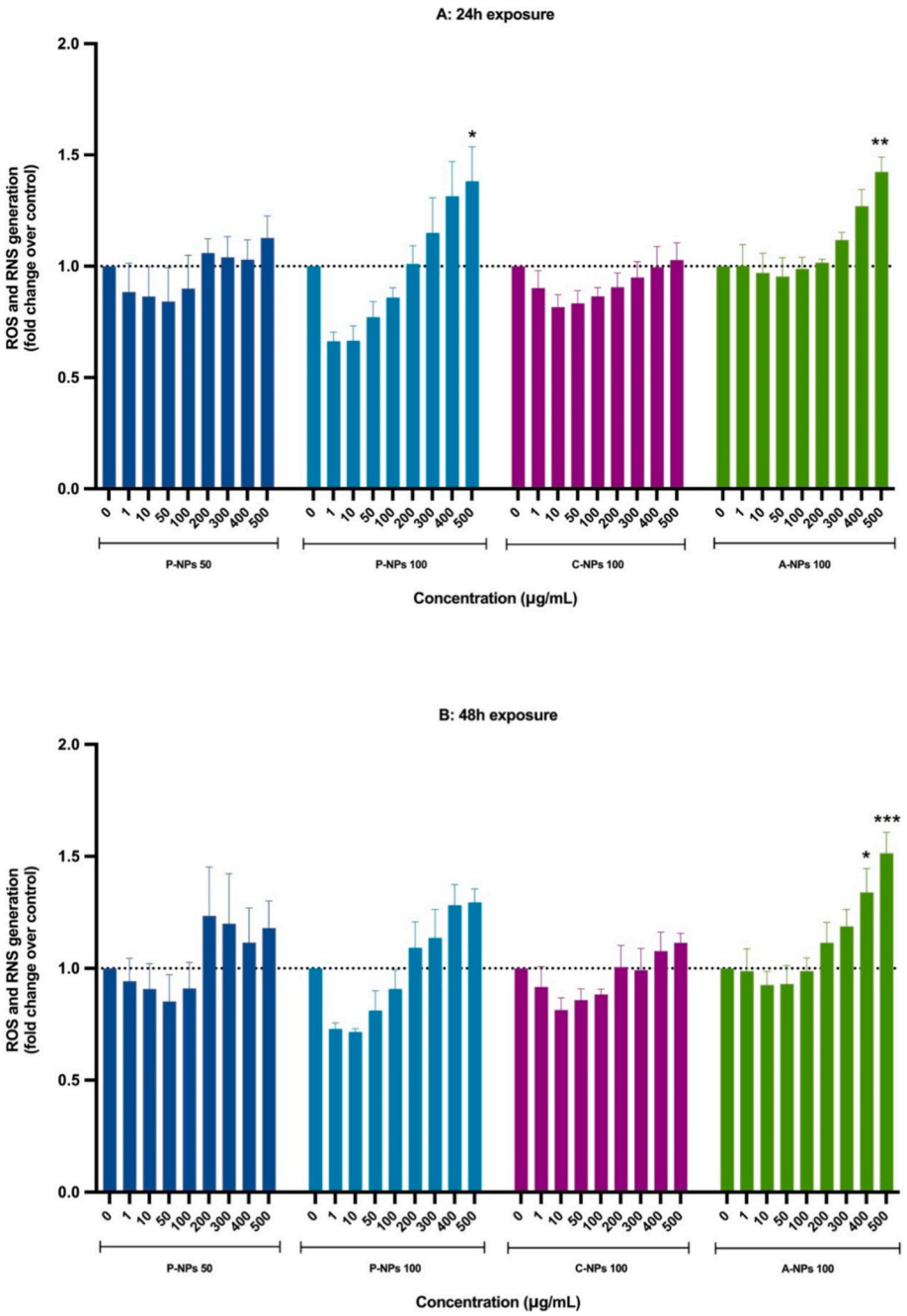

Fig. 4. Generation of ROS and RNS in SH-SY5Y cells exposed to plain and functionalized PS-NPs. SH-SY5Y cells were treated with increasing concentrations (1–500 µg/mL) of 50 nm plain NPs (dark blue), 100 nm plain NPs (light blue), 100 nm carboxyl-functionalized NPs (purple), 100 nm amine-functionalized NPs (green) for **(A)** 24 and **(B)** 48 h. Data are presented as mean ± standard error of the mean (SEM) (n = 5, except n = 4 for 50 nm and 100 nm plain NPs). *$p < 0.05$, **$p < 0.01$, ***$p < 0.001$ vs. control. (For interpretation of the references to color in this figure legend, the reader is referred to the Web version of this article.)

These findings align with earlier evidence that charged surfaces enhance cell–membrane interactions (Banerjee et al., 2021; Li & Malmstadt, 2013).

Ultrastructural analysis showed preserved morphology in controls, including mitochondria with intact cristae, rough ER (RER), and normal vacuoles. NP-treated cells displayed organelle-specific alterations varying by particle type and concentration. RER dilatation was common except with A-NPs 100, suggesting disruption of protein synthesis/homeostasis (Guo et al., 2024), consistent with prior links between NPs and ER stress (Halimu et al., 2022; Jeon et al., 2023).

Mitochondria were particularly affected. P-NPs 50 reduced mitochondrial numbers without visible damage, whereas P-NPs 100 reduced counts and caused structural injury. C-NPs 100 preserved overall numbers but increased abnormal mitochondria, implying impaired quality control. A-NPs 100 induced mitochondrial biogenesis but also more abnormal forms, indicating a compensatory yet insufficient response. Such dysfunction may impair ATP production, elevate ROS, activate apoptosis, and disrupt signaling (Brillo et al., 2021). Consistently, Hoechst/PI staining confirmed apoptosis as the primary death pathway, with stronger responses in A- and C-NP-treated cells. Functionalized NP cytotoxicity was time- and concentration-dependent and consistent with *in vivo* evidence of A-NPs 100-induced apoptosis via the p53/Bax/Bcl-2 pathway (Bai et al., 2024; Y. Ma et al., 2024; Shan et al., 2022). Similarly, PS-NPs (40–60 nm) penetrate membranes, accumulate

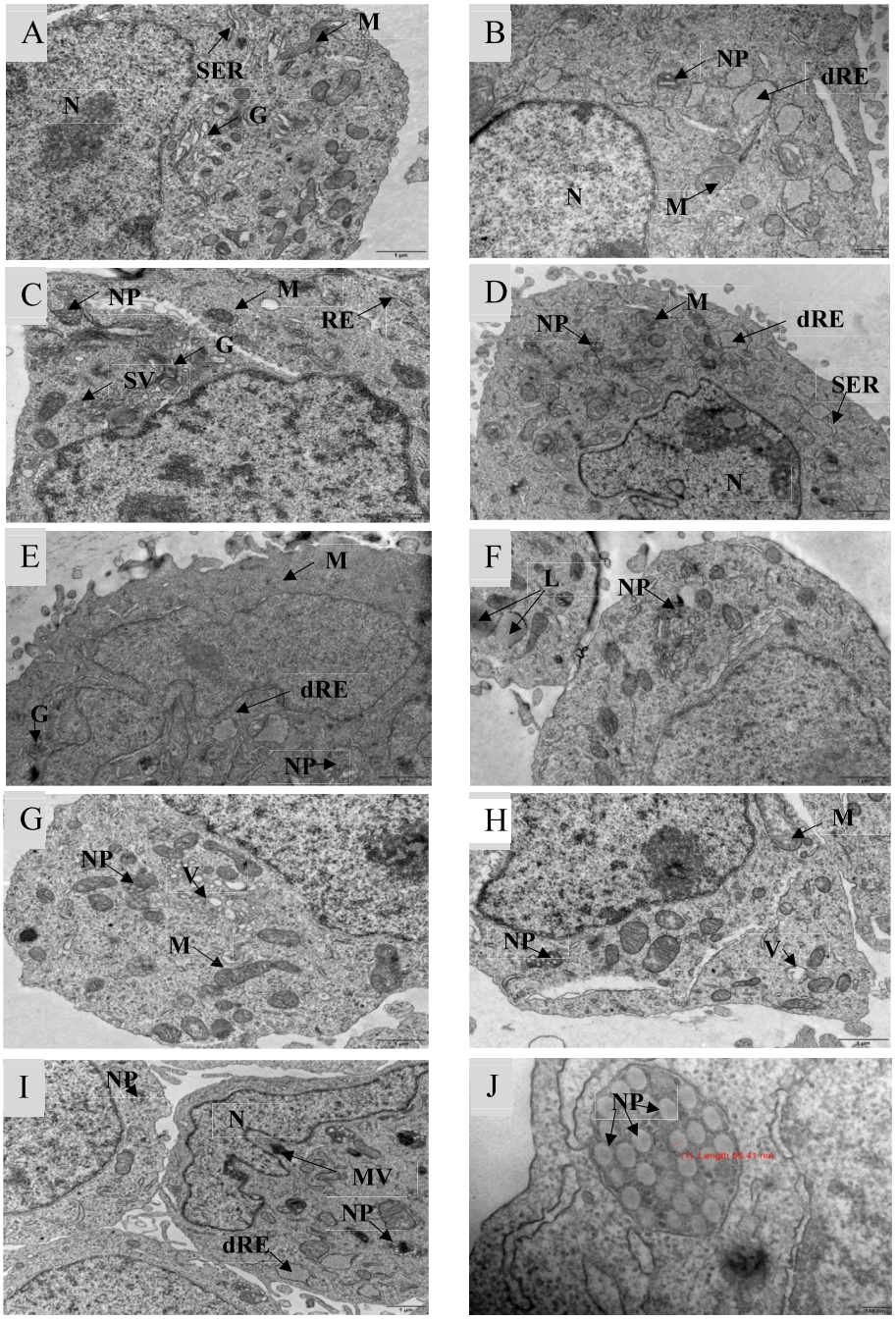

Fig. 5. Representative TEM images of neuronal SH-SY5Y cells exposed to plain and functionalized PS-NPs. (A) Control (untreated cells), (B) P-NPs 50 (50 μg/ml), (C) P-NPs 50 (200 μg/ml), (D) P-NPs 100 (50 μg/ml), (E) P-NPs 100 (200 μg/ml), (F) A-NPs 100 (50 μg/ml), (G) A-NPs 100 (200 μg/ml), (H) C-NPs 100 (50 μg/ml), (I) C-NPs 100 (200 μg/ml), (J) representative vesicles containing NPs (blue stars). Images were acquired using a JEOL JEM 1400 transmission electron microscope. G - golgi apparatus, L - lipid droplets, M - mitochondria, N - nucleus, RER - rough endoplasmic reticulum, dRER - dilated rough endoplasmic reticulum, SER - smooth endoplasmic reticulum, V - vacuole, SV - small vesicles, MVB - multivesicular bodies, NP - nanoplastics.

in mitochondria, and trigger apoptosis in human cerebral organoids (Kari et al., 2022). Our findings differ from Huang et al. (2023), who observed severe mitochondrial damage with P-NPs 50, likely due to exposure differences. Importantly, no prior studies have examined functionalized NP effects on neuronal mitochondrial integrity, underscoring a key knowledge gap.

Golgi apparatus disruption—fragmentation, swelling, dilation—was evident in all NP-treated cells, most prominently with functionalized NPs. Such alterations may impair protein trafficking/secretion (Mohan et al., 2023) and contribute to stress, potentially triggering autophagy and lysosomal responses. Multivesicular bodies and autophagic vacuoles were frequent, strongest in A-NPs 100-treated cells, followed by C-NPs 100 and P-NPs 100. P-NPs 50 did not elicit autophagy, contrasting with Tang et al. (2022), who reported upregulation under higher exposures. Autophagy likely acts protectively by degrading damaged organelles or aggregates, particularly with functionalized NPs, but prolonged activation may worsen stress and promote cell death (Li et al., 2024). This dual role aligns with prior reports of PS-NPs enhancing lysosomal translocation or impairing autophagic flux despite activation (Han et al., 2024; Kobayashi et al., 2010; Liu et al., 2024; Song et al., 2015).

Lysosomal dysfunction, indicated by vacuolar alterations and electron-dense vesicles, was most evident in P-NPs 100- and C-NPs 100-

Table 1
Semi-quantitative transmission electron microscopy (TEM) analysis of SH-SY5Y cells exposed to different types of PS-NPs with distinct surface functionalizations (plain, carboxylated, and aminated) at 50 and 200 μg/mL for 24 h. The table summarizes the presence of NPs, number of lipid droplets, total and abnormal number of mitochondria, and qualitative alterations in subcellular organelles (Golgi apparatus, rough endoplasmic reticulum, vacuoles, small vesicles, and multivesicular bodies/autophagy vacuoles). The color scale indicates the relative level of structural alterations: blue = low, green = moderate, red = high. "Dil." indicates organelle dilation.

Area (3806,00 μm²)	Presence of NPs	Nº of lipid droplets	Nº of total mitochondria	Nº of abnormal mitochondria	Golgi apparatus	Rough endoplasmic reticulum	Vacuoles	Small vesicles	Multivesicular bodies/autophagy vacuoles
Control	0	17	231	0	🔵	present, normal	normal	normal	normal
P-NPs 50 (50 μg/mL)	🔵	17	131	0	🔵	dil 🟢	normal	🔵	normal
P-NPs 50 (200 μg/mL)	🔵	20	194	0	🔵	dil 🟢	🔵	🟢	normal
P-NPs 100 (50 μg/mL)	🔵	47	178	🔵	🔵	dil 🔴	🟢	🟢	🔵
P-NPs 100 (200 μg/mL)	🔵	67	188	🔵	🟢	dil 🟢	🟢	🟢	🔵
C-NPs 100 (50 μg/mL)	🟢	23	298	🔵	🔴	dil 🟢	🟢	🔴	🔵
C-NPs 100 (200 μg/mL)	🟢	25	236	🔵	🔴	dil 🟢	🟢	🔴	🔵
A-NPs 100 (50 μg/mL)	🔴	21	379	🟢	🟢	present	🔵	🔵	🟢
A-NPs 100 (200 μg/mL)	🔴	31	263	🟢	🟢	present	🔵	🟢	🟢

Note: dil, dilated; 🔵 Low expression level; 🟢 Moderate expression level; 🔴 High expression level

treated cells, with similar changes in A-NPs 100 and P-NPs 50 at higher doses. These alterations, together with electron-dense vacuoles, lysosomes, and multivesicular bodies, suggest PS-NPs impair lysosomal function. Such patterns, consistent with prior findings in Caco-2 (Domenech et al., 2021) and astrocytoma cells (Wang et al., 2013), indicate lysosomal NP accumulation may cause irreversible storage, damage, and enhanced cytotoxicity (Salvati et al., 2011).

3.6. Integrative mechanism of PS-NP neurotoxicity

This study provides an integrative view of PS-NP neurotoxicity by linking physicochemical properties, serum-dependent colloidal behavior, and organelle-level responses in human neuronal cells. The results demonstrate that surface functionalization dictates neuronal stress via electrostatic uptake, ER–mitochondrial crosstalk, and autophagy–lysosome disruption, advancing mechanistic understanding beyond traditional cytotoxicity and oxidative stress endpoints.

Upon dispersion in low-serum medium, all PS-NPs form a stabilizing protein corona that preserves surface features critical for membrane recognition. The higher cytotoxicity of amine-functionalized PS-NPs stems from electrostatic attraction between partially protonated amine groups and the anionic neuronal membrane, enhancing uptake and lysosomal accumulation. Internalized particles activate three main stress axes: ER dilation triggers an unfolded-protein response; mitochondrial dysfunction impairs ATP homeostasis and increases oxidative stress; and Golgi fragmentation disrupts vesicular trafficking. In A-NPs 100, these pathways act simultaneously with a strong oxidative-nitrosative burst, whereas C-NPs 100 follow the same sequence but with lower uptake and limited redox imbalance. Plain particles induce only minor effects, constrained by reduced internalization and extracellular aggregation. Overall, these findings support a model in which surface chemistry modulates both the intensity and pathway of neuronal injury, aligning with recent *in vivo* evidence (Y. Ma et al., 2024; Bai et al., 2024). The proposed integrative mechanism of PS-NP neurotoxicity is summarized in Fig. 6.

Despite the robustness of our findings, this study has limitations. Functionalized PS-NPs of 50 nm were not commercially available, which precluded a fully orthogonal assessment of size versus surface chemistry. Nevertheless, the overall trends observed between plain and functionalized PS-NPs (100 nm) remain consistent with surface chemistry being a dominant factor of neurotoxic responses. Future studies could address this gap by applying controlled post-synthesis functionalization methods—such as covalent grafting, plasma modification, or carbodiimide-mediated coupling—to generate smaller functionalized NPs and enable more systematic mechanistic comparisons. The exclusive use of PS as the model polymer also limits generalizability, as different polymer matrices may influence NP behavior and hazard potential. Furthermore, the proposed mechanisms of ER stress, mitochondrial dysfunction, and autophagy–lysosome impairment are inferred from consistent ultrastructural hallmarks observed by TEM, including ER dilation, mitochondrial swelling, and accumulation of autophagic vacuoles. While these morphological patterns strongly suggest activation of stress pathways, they should be regarded as hypothesis-generating until confirmed by molecular endpoints (e.g., CHOP for ER stress, LC3B-II/p62 for autophagy, Bax/Bcl-2 for apoptosis). Future studies incorporating such molecular assays will be essential to validate and expand these mechanistic insights. Long-term studies remain necessary to clarify neurotoxic risks associated with increasing environmental NP exposure.

4. Conclusions

This study provides a comprehensive evaluation of PS-NP neurotoxicity in SH-SY5Y cells and highlights the critical role of FBS concentration in nanoparticle stability, aggregation, surface charge, and biological interactions. Our findings emphasize the need to standardize FBS conditions to ensure reproducibility in *in vitro* toxicity assessments. We further show that surface-functionalized PS-NPs, particularly amine-modified forms, induce stronger, time-dependent cytotoxicity than non-functionalized particles, driven by enhanced uptake and mechanisms

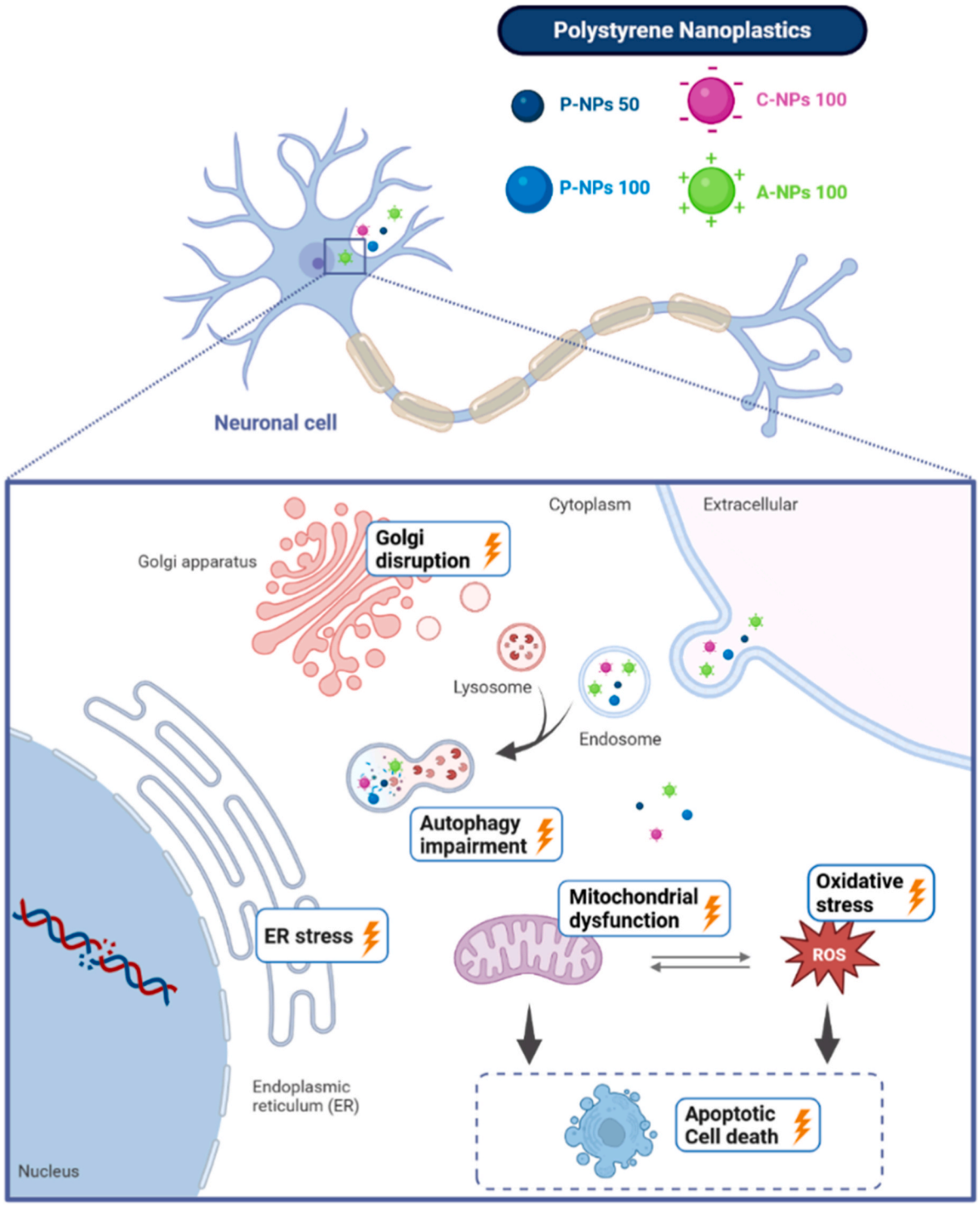

Fig. 6. Putative mechanisms of PS-NPs-induced toxicity in neuronal SH-SY5Y cells. Created in https://BioRender.com.

involving oxidative stress, membrane disruption, mitochondrial dysfunction, and impaired autophagy–lysosome activity. From an environmental perspective, these results underscore the urgency of establishing standardized protocols for nanoplastic toxicity testing, as small variations in experimental design may obscure or overstate potential risks. Given the widespread occurrence of plastic-derived nanoparticles and their potential to affect the nervous system, long-term, mechanistically informed studies are essential to strengthen human health risk assessment. Incorporating such mechanistic insights into regulatory frameworks will be critical for managing the emerging threat of nanoplastic pollution.

CRediT authorship contribution statement

Carolina Mota: Writing – original draft, Investigation. **Ana Margarida Araújo:** Writing – review & editing, Supervision, Software, Formal analysis, Conceptualization. **Maria Enea:** Writing – review & editing, Investigation. **Eulália Pereira:** Writing – review & editing. **Ana Reis-Mendes:** Writing – review & editing, Investigation. **Rui Fernandes:** Writing – review & editing, Methodology, Investigation. **Sofia Pacheco:** Writing – review & editing, Methodology, Investigation. **Marlene Lúcio:** Writing – review & editing, Methodology, Investigation. **Carla Martins Lopes:** Writing – review & editing, Methodology,

Investigation. **Isabel M.P.L.V.O. Ferreira:** Writing – review & editing, Supervision, Resources, Funding acquisition. **Márcia Carvalho:** Writing – review & editing, Visualization, Validation, Supervision, Methodology, Investigation, Formal analysis, Data curation, Conceptualization.

Funding

This work was supported by FCT/MCTES, through the SALIVA + project (DOI 705 10.54499/2022.08978.PTDC). This work was also supported by the PT national funds (FCT/MECI) through the project UID/50006 - Laboratório Associado para a Química Verde - Tecnologias e Processos Limpos and the Strategic Funding UIDB/04650/2020 and UIDB/04050/2020 (CF-UM-UP and CBMA), UIDP/04378/2020 and UIDB/04378/2020 (UCIBIO) and the project LA/P/0140/2020 (i4HB).

Declaration of competing interest

The authors declare that they have no known competing financial interests or personal relationships that could have appeared to influence the work reported in this paper.

Acknowledgement

The authors acknowledge the support of the i3S Scientific Platform HEMS, member of the national infrastructure PPBI - Portuguese Platform of Bioimaging (PPBI-POCI-01-0145-FEDER-022122).

Appendix A. Supplementary data

Supplementary data to this article can be found online at https://doi.org/10.1016/j.envpol.2025.127445.

Data availability

Data will be made available on request.

References

Abbasi, R., Shineh, G., Mobaraki, M., Doughty, S., Tayebi, L., 2023. Structural parameters of nanoparticles affecting their toxicity for biomedical applications: a review. J. Nanoparticle Res. 25 (3), 43.

Akhter, M.H., Khalilullah, H., Gupta, M., Alfaleh, M.A., Alhakamy, N.A., Riadi, Y., Md, S., 2021. Impact of protein Corona on the biological identity of nanomedicine: understanding the fate of nanomaterials in the biological milieu. Biomedicines 9 (10).

Allouni, Z.E., Cimpan, M.R., Høl, P.J., Skodvin, T., Gjerdet, N.R., 2009. Agglomeration and sedimentation of TiO2 nanoparticles in cell culture medium. Colloids Surf. B Biointerfaces 68 (1), 83–87.

Anders, C.B., Chess, J.J., Wingett, D.G., Punnoose, A., 2015. Serum proteins enhance dispersion stability and influence the cytotoxicity and dosimetry of ZnO nanoparticles in suspension and adherent cancer cell models. Nanoscale Res. Lett. 10 (1), 448.

Bai, H., Wu, Y., Li, H., Zhu, Y., Che, R., Wang, F., Zhang, C., 2024. Cerebral neurotoxicity of amino-modified polystyrene nanoplastics in mice and the protective effects of functional food camellia pollen. Sci. Total Environ. 912, 169511.

Ban, M., Shimoda, R., Chen, J., 2021. Investigation of nanoplastic cytotoxicity using SH-SY5Y human neuroblastoma cells and polystyrene nanoparticles. Toxicol. Vitro 76, 105225.

Banerjee, A., Billey, L.O., Shelver, W.L., 2021. Uptake and toxicity of polystyrene micro/nanoplastics in gastric cells: effects of particle size and surface functionalization. PLoS One 16 (12), e0260803.

Bhattacharjee, S., 2016. DLS and zeta potential - what they are and what they are not? J Control Release 235, 337–351.

Brar, S.K., Verma, M., 2011. Measurement of nanoparticles by light-scattering techniques. TrAC, Trends Anal. Chem. 30 (1), 4–17.

Brillo, V., Chieregato, L., Leanza, L., Muccioli, S., Costa, R., 2021. Mitochondrial dynamics, ROS, and cell signaling: a blended overview. Life 11 (4), 332.

Brits, M., van Velzen, M.J.M., Sefiloglu, F.Ö., Scibetta, L., Groenewoud, Q., Garcia-Vallejo, J.J., Vethaak, A.D., Brandsma, S.H., Lamoree, M.H., 2024. Quantitation of micro and nanoplastics in human blood by pyrolysis-gas chromatography–mass spectrometry. Microplastics and Nanoplastics 4 (1), 12.

Conesa, J.A., Iñiguez, M.E., 2020. Analysis of microplastics in food samples. Handbook of Microplastics in the Environment 1–16.

Danaei, M., Dehghankhold, M., Ataei, S., Hasanzadeh Davarani, F., Javanmard, R., Dokhani, A., Khorasani, S., Mozafari, M.R., 2018. Impact of particle size and polydispersity index on the clinical applications of lipidic nanocarrier systems. Pharmaceutics 10 (2).

Domenech, J., de Britto, M., Velázquez, A., Pastor, S., Hernández, A., Marcos, R., Cortés, C., 2021. Long-term effects of polystyrene nanoplastics in human intestinal Caco-2 cells. Biomolecules 11 (10), 1442.

Enders, K., Lenz, R., Stedmon, C.A., Nielsen, T.G., 2015. Abundance, size and polymer composition of marine microplastics≥ 10 μm in the Atlantic Ocean and their modelled vertical distribution. Mar. Pollut. Bull. 100 (1), 70–81.

Feng, Y., Tu, C., Li, R., Wu, D., Yang, J., Xia, Y., Peijnenburg, W.J., Luo, Y., 2023. A systematic review of the impacts of exposure to micro-and nano-plastics on human tissue accumulation and health. Eco-Environ. Health. 2 (4), 195–207.

Fleischer, C.C., Payne, C.K., 2014. Nanoparticle–cell interactions: molecular structure of the protein corona and cellular outcomes. Acc. Chem. Res. 47 (8), 2651–2659.

Fu, L., Li, J., Wang, G., Luan, Y., Dai, W., 2021. Adsorption behavior of organic pollutants on microplastics. Ecotoxicology and environmental safety 217, 112207.

Guo, X., Lin, H., Xu, S., He, L., 2022. Recent advances in spectroscopic techniques for the analysis of microplastics in food. J. Agric. Food Chem. 70 (5), 1410–1422.

Guo, Z., Chi, R., Peng, Y., Sun, K., Liu, H., Guo, F., Guo, J., 2024. The role and interactive mechanism of endoplasmic reticulum stress and ferroptosis in musculoskeletal disorders. Biomolecules 14 (11), 1369.

Halimu, G., Zhang, Q., Liu, L., Zhang, Z., Wang, X., Gu, W., Zhang, B., Dai, Y., Zhang, H., Zhang, C., 2022. Toxic effects of nanoplastics with different sizes and surface charges on epithelial-to-mesenchymal transition in A549 cells and the potential toxicological mechanism. J. Hazard Mater. 430, 128485.

Han, S.W., Choi, J., Ryu, K.Y., 2024. Recent progress and future directions of the research on nanoplastic-induced neurotoxicity. Neural Regen. Res. 19 (2), 331–335.

He, J., Fu, X., Ni, F., Yang, G., Deng, S., Chen, J.P., Shen, F., 2022. Quantitative assessment of interactions of hydrophilic organic contaminants with microplastics in natural water environment. Water Res. 224, 119024.

Hu, K., Yang, Y., Zuo, J., Tian, W., Wang, Y., Duan, X., Wang, S., 2022. Emerging microplastics in the environment: properties, distributions, and impacts. Chemosphere 297, 134118.

Huang, Y., Liang, B., Li, Z., Zhong, Y., Wang, B., Zhang, B., Du, J., Ye, R., Xian, H., Min, W., 2023. Polystyrene nanoplastic exposure induces excessive mitophagy by activating AMPK/ULK1 pathway in differentiated SH-SY5Y cells and dopaminergic neurons in vivo. Part. Fibre Toxicol. 20 (1), 44.

Hwang, J., Choi, D., Han, S., Jung, S.Y., Choi, J., Hong, J., 2020. Potential toxicity of polystyrene microplastic particles. Sci. Rep. 10 (1), 7391.

Jeon, M.S., Kim, J.W., Han, Y.B., Jeong, M.H., Kim, H.R., Sik Kim, H., Park, Y.J., Chung, K.H., 2023. Polystyrene microplastic particles induce autophagic cell death in BEAS-2B human bronchial epithelial cells. Environ. Toxicol. 38 (2), 359–367.

Ji, S., Wang, W., Wang, Y., Bai, H., Li, Z., Huo, Z., Luo, K., 2025. Quantitative detection of Micro- and nanoplastics (≥300 nm) in human urine using double-shot Py-GC/MS with internal standard calibration. Toxics 13 (6).

Jiang, J., Oberdörster, G., Biswas, P., 2009. Characterization of size, surface charge, and agglomeration state of nanoparticle dispersions for toxicological studies. J. Nanoparticle Res. 11 (1), 77–89.

Jin, M., Wang, X., Ren, T., Wang, J., Shan, J., 2021. Microplastics contamination in food and beverages: direct exposure to humans. J. Food Sci. 86 (7), 2816–2837.

Kadac-Czapska, K., Knez, E., Grembecka, M., 2024. Food and human safety: the impact of microplastics. Crit. Rev. Food Sci. Nutr. 64 (11), 3502–3521.

Kari, S., Subramanian, K., Altomonte, I.A., Murugesan, A., Yli-Harja, O., Kandhavelu, M., 2022. Programmed cell death detection methods: a systematic review and a categorical comparison. Apoptosis 27 (7–8), 482–508.

Kobayashi, S., Kojidani, T., Osakada, H., Yamamoto, A., Yoshimori, T., Hiraoka, Y., Haraguchi, T., 2010. Artificial induction of autophagy around polystyrene beads in nonphagocytic cells. Autophagy 6 (1), 36–45.

Kopac, T., 2021. Protein Corona, understanding the nanoparticle–protein interactions and future perspectives: a critical review. Int. J. Biol. Macromol. 169, 290–301.

Leslie, H.A., van Velzen, M.J.M., Brandsma, S.H., Vethaak, A.D., Garcia-Vallejo, J.J., Lamoree, M.H., 2022. Discovery and quantification of plastic particle pollution in human blood. Environ. Int. 163, 107199.

Li, J., Weng, H., Liu, S., Li, F., Xu, K., Wen, S., Chen, X., Li, C., Nie, Y., Liao, B., 2024. Embryonic exposure of polystyrene nanoplastics affects cardiac development. Sci. Total Environ. 906, 167406.

Li, S., Malmstadt, N., 2013. Deformation and poration of lipid bilayer membranes by cationic nanoparticles. Soft Matter 9 (20), 4969–4976.

Lin, S., Zhang, H., Wang, C., Su, X.-L., Song, Y., Wu, P., Yang, Z., Wong, M.-H., Cai, Z., Zheng, C., 2022. Metabolomics reveal nanoplastic-induced mitochondrial damage in human liver and lung cells. Environ. Sci. Technol. 56 (17), 12483–12493.

Liu, Q., Chen, Z., Chen, Y., Yang, F., Yao, W., Xie, Y., 2021. Microplastics and nanoplastics: emerging contaminants in food. J. Agric. Food Chem. 69 (36), 10450–10468.

Liu, S., He, Y., Yin, J., Zhu, Q., Liao, C., Jiang, G., 2024. Neurotoxicities induced by micro/nanoplastics: a review focusing on the risks of neurological diseases. J. Hazard Mater., 134054

Liu, S., Li, Y., Shang, L., Yin, J., Qian, Z., Chen, C., Yang, Y., 2022. Size-dependent neurotoxicity of micro-and nanoplastics in flowing condition based on an in vitro microfluidic study. Chemosphere 303, 135280.

Liu, X., Xu, J., Zhao, Y., Shi, H., Huang, C.-H., 2019. Hydrophobic sorption behaviors of 17β-Estradiol on environmental microplastics. Chemosphere 226, 726–735.

Ma, L., Wu, Z., Lu, Z., Yan, L., Dong, X., Dai, Z., Sun, R., Hong, P., Zhou, C., Li, C., 2024. Differences in toxicity induced by the various polymer types of nanoplastics on HepG2 cells. Sci. Total Environ. 918, 170664.

Ma, Y., Xu, D., Wan, Z., Wei, Z., Chen, Z., Wang, Y., Han, X., Chen, Y., 2024. Exposure to different surface-modified polystyrene nanoparticles caused anxiety, depression, and social deficit in mice via damaging mitochondria in neurons. Sci. Total Environ. 919, 170739.
Maity, S., Guchhait, R., Sarkar, M.B., Pramanick, K., 2022. Occurrence and distribution of micro/nanoplastics in soils and their phytotoxic effects: a review. Plant Cell Environ. 45 (4), 1011–1028.
Materić, D., Peacock, M., Dean, J., Futter, M., Maximov, T., Moldan, F., Röckmann, T., Holzinger, R., 2022. Presence of nanoplastics in rural and remote surface waters. Environ. Res. Lett. 17 (5), 054036.
Mohan, A.G., Calenic, B., Ghiurau, N.A., Duncea-Borca, R.-M., Constantinescu, A.-E., Constantinescu, I., 2023. The golgi apparatus: a voyage through time, structure, function and implication in neurodegenerative disorders. Cells 12 (15), 1972.
Monopoli, M.P., Aberg, C., Salvati, A., Dawson, K.A., 2012. Biomolecular coronas provide the biological identity of nanosized materials. Nat. Nanotechnol. 7 (12), 779–786.
Mortensen, N.P., Caffaro, M.M., Krovi, A., Kim, J., Watson, S.L., Snyder, R.W., Patel, P.R., Fennell, T.R., Johnson, L.M., 2025. Oral exposure to Nylon-11 and polystyrene nanoplastics during early-life in rats. Nanomaterials 15 (6).
Nihart, A.J., Garcia, M.A., El Hayek, E., Liu, R., Olewine, M., Kingston, J.D., Castillo, E.F., Gullapalli, R.R., Howard, T., Bleske, B., 2025. Bioaccumulation of microplastics in decedent human brains. Nat. Med. 1–6.
Okoffo, E.D., Thomas, K.V., 2024. Quantitative analysis of nanoplastics in environmental and potable waters by pyrolysis-gas chromatography-mass spectrometry. J. Hazard Mater. 464, 133013.
Patil, S.M., Rane, N.R., Bankole, P.O., Krishnaiah, P., Ahn, Y., Park, Y.-K., Yadav, K.K., Amin, M.A., Jeon, B.-H., 2022. An assessment of micro-and nanoplastics in the biosphere: a review of detection, monitoring, and remediation technology. Chem. Eng. J. 430, 132913.
Petersen, E.J., Barrios, A.C., Henry, T.B., Johnson, M.E., Koelmans, A.A., Montoro Bustos, A.R., Matheson, J., Roesslein, M., Zhao, J., Xing, B., 2022. Potential artifacts and control experiments in toxicity tests of nanoplastic and microplastic particles. Environ. Sci. Technol. 56 (22), 15192–15206.
Peula-García, J.M., Ortega-Vinuesa, J.L., Bastos-González, D., 2010. Inversion of hofmeister series by changing the surface of colloidal particles from hydrophobic to hydrophilic. J. Phys. Chem. C 114 (25), 11133–11139.
Pironti, C., Ricciardi, M., Motta, O., Miele, Y., Proto, A., Montano, L., 2021. Microplastics in the environment: intake through the food web, human exposure and toxicological effects. Toxics 9 (9), 224.
Prüst, M., Meijer, J., Westerink, R.H., 2020. The plastic brain: neurotoxicity of micro-and nanoplastics. Part. Fibre Toxicol. 17, 1–16.
Rahman, M., Laurent, S., Tawil, N., Yahia, L.H., Mahmoudi, M., Rahman, M., Laurent, S., Tawil, N., Yahia, L.H., Mahmoudi, M., 2013. Nanoparticle and protein corona. Protein-Nanoparticle Interactions: The Bio-Nano Interface 21–44.
Salvati, A., Åberg, C., dos Santos, T., Varela, J., Pinto, P., Lynch, I., Dawson, K.A., 2011. Experimental and theoretical comparison of intracellular import of polymeric nanoparticles and small molecules: toward models of uptake kinetics. Nanomed. Nanotechnol. Biol. Med. 7 (6), 818–826.
Shan, S., Zhang, Y., Zhao, H., Zeng, T., Zhao, X., 2022. Polystyrene nanoplastics penetrate across the blood-brain barrier and induce activation of microglia in the brain of mice. Chemosphere 298, 134261.
Shi, X., Wang, X., Huang, R., Tang, C., Hu, C., Ning, P., Wang, F., 2022. Cytotoxicity and genotoxicity of polystyrene micro-and nanoplastics with different size and surface modification in A549 cells. Int. J. Nanomed. 17, 4509.
Song, W., Popp, L., Yang, J., Kumar, A., Gangoli, V.S., Segatori, L., 2015. The autophagic response to polystyrene nanoparticles is mediated by transcription factor EB and depends on surface charge. J. Nanobiotechnol. 13, 1–12.
Souza, T.G.F., Ciminelli, V.S.T., Mohallem, N.D.S., 2016. A comparison of TEM and DLS methods to characterize size distribution of ceramic nanoparticles. J. Phys. Conf. 733.
Sun, Y., Devore, D., Ma, X., Yuan, Y., Kohn, J., Qian, J., 2019. Promotion of dispersion and anticancer efficacy of hydroxyapatite nanoparticles by the adsorption of fetal bovine serum. J. Nanoparticle Res. 21, 1–12.
Süssmann, J., Krause, T., Fischer, E.K., Walz, E., Greiner, R., Rohn, S., Fritsche, J., 2026. Microplastics in fresh and processed seafood – a survey of products sold in Germany. Food Control 179, 111565.
Tallec, K., Blard, O., González-Fernández, C., Brotons, G., Berchel, M., Soudant, P., Huvet, A., Paul-Pont, I., 2019. Surface functionalization determines behavior of nanoplastic solutions in model aquatic environments. Chemosphere 225, 639–646.
Tang, Q., Li, T., Chen, K., Deng, X., Zhang, Q., Tang, H., Shi, Z., Zhu, T., Zhu, J., 2022. PS-NPs induced neurotoxic effects in SHSY-5Y cells via autophagy activation and mitochondrial dysfunction. Brain Sci. 12 (7), 952.
Valente, M.J., Henrique, R., Vilas-Boas, V., Silva, R., Bastos, M.d.L., Carvalho, F., Guedes de Pinho, P., Carvalho, M., 2012. Cocaine-induced kidney toxicity: an in vitro study using primary cultured human proximal tubular epithelial cells. Arch. Toxicol. 86, 249–261.
Verla, A.W., Enyoh, C.E., Verla, E.N., Nwarnorh, K.O., 2019. Microplastic–toxic chemical interaction: a review study on quantified levels, mechanism and implication. SN Appl. Sci. 1 (11), 1–30.
Wang, F., Bexiga, M.G., Anguissola, S., Boya, P., Simpson, J.C., Salvati, A., Dawson, K.A., 2013. Time resolved study of cell death mechanisms induced by amine-modified polystyrene nanoparticles. Nanoscale 5 (22), 10868–10876.
Wang, H., Shi, X., Gao, Y., Zhang, X., Zhao, H., Wang, L., Zhang, X., Chen, R., 2022. Polystyrene nanoplastics induce profound metabolic shift in human cells as revealed by integrated proteomic and metabolomic analysis. Environ. Int. 166, 107349.
Xu, M., Halimu, G., Zhang, Q., Song, Y., Fu, X., Li, Y., Li, Y., Zhang, H., 2019. Internalization and toxicity: a preliminary study of effects of nanoplastic particles on human lung epithelial cell. Sci. Total Environ. 694, 133794.
Xu, Y., Ou, Q., van der Hoek, J.P., Liu, G., Lompe, K.M., 2024. Photo-oxidation of Micro- and nanoplastics: physical, chemical, and biological effects in environments. Environ. Sci. Technol. 58 (2), 991–1009.
Yang, H., Chen, G., Wang, J., 2021. Microplastics in the marine environment: sources, fates, impacts and microbial degradation. Toxics 9 (2).
Yang, S., Lee, S., Lee, Y., Cho, J.-H., Kim, S.H., Ha, E.-S., Jung, Y.-S., Chung, H.Y., Kim, M.-S., Kim, H.S., 2023. Cationic nanoplastic causes mitochondrial dysfunction in neural progenitor cells and impairs hippocampal neurogenesis. Free Radic. Biol. Med. 208, 194–210.
Yeo, E.L.L., Chua, A.J.S., Parthasarathy, K., Yeo, H.Y., Ng, M.L., Kah, J.C.Y., 2015. Understanding aggregation-based assays: nature of protein corona and number of epitopes on antigen matters. RSC Adv. 5 (20), 14982–14993.
Zhang, P., Chen, D., Li, L., Sun, K., 2022. Charge reversal nano-systems for tumor therapy. J. Nanobiotechnol. 20 (1), 31.
Zhang, X., Zheng, M., Yin, X., Wang, L., Lou, Y., Qu, L., Liu, X., Zhu, H., Qiu, Y., 2019. Sorption of 3, 6-dibromocarbazole and 1, 3, 6, 8-tetrabromocarbazole by microplastics. Mar. Pollut. Bull. 138, 458–463.